The Astrophysical Journal, 983:142 (10pp), 2025 April 20 https://doi.org/10.3847/1538-4357/adc253

First Measurement of ^{87}Rb(α, xn) Cross Sections at Weak r-process Energies in Supernova ν-driven Ejecta to Investigate Elemental Abundances in Low-metallicity Stars

C. Fougères[1,2,3], M. L. Avila[1], A. Psaltis[4,5], M. Anastasiou[6], S. Bae[7], L. Balliet[8], K. Bhatt[1], L. Dienis[9], H. Jayatissa[10], V. Karayonchev[1], P. Mohr[11], F. Montes[8], D. Neto[1,12], F. de Oliveira Santos[9], W.-J. Ong[6], K. E. Rehm[1], W. Reviol[1], D. Santiago-Gonzalez[1], N. Sensharma[1], R. S. Sidhu[13], and I. A. Tolstukhin[1]
[1] Physics Division, Argonne National Laboratory Lemont, IL 60439, USA; chloe.fougeres@cea.fr
[2] CEA, DAM, DIF, 91297 Arpajon, France
[3] Laboratoire Matiére en Conditions Extrêmes, Universitè Paris-Saclay, CEA, 91680 Bruyères-le-Châtel, France
[4] Department of Physics, Duke University, Durham, NC 27710, USA
[5] Triangle Universities Nuclear Laboratory, Duke University, Durham, NC 27710, USA
[6] Nuclear and Chemical Sciences Division, Lawrence Livermore National Laboratory, Livermore, CA 94550, USA
[7] Center for Exotic Nuclear Studies, Institute for Basic Science, Daejeon, 34126, Republic of Korea
[8] Facility for Rare Isotope Beams (FRIB), Michigan State University, East Lansing, MI 48824, USA
[9] Grand Accélérateur National d'Ions Lourds (GANIL), Caen, France
[10] Physics Division, Los Alamos National Laboratory, NM 87545, USA
[11] HUN-REN Institute for Nuclear Research (ATOMKI), H-4001 Debrecen, Hungary
[12] Department of Physics, University of Illinois Chicago, 845 W. Taylor St., Chicago, IL 60607, USA
[13] School of Mathematics and Physics, University of Surrey, Guildford, GU2 7XH, UK
Received 2025 February 15; revised 2025 March 13; accepted 2025 March 17; published 2025 April 16

Abstract

Observed abundances of $Z \sim 40$ elements in metal-poor stars vary from star to star, indicating that the rapid and slow neutron capture processes may not contribute alone to the synthesis of elements beyond iron. The weak r-process was proposed to produce $Z \sim 40$ elements in a subset of old stars. Thought to occur in the ν-driven ejecta of a core-collapse supernova, (α, xn) reactions would drive the nuclear flow toward heavier masses at $T = 2-5$ GK. However, current comparisons between modeled and observed yields do not bring satisfactory insights into the stellar environment, mainly due to the uncertainties of the nuclear physics inputs where the dispersion in a given reaction rate often exceeds 1 order of magnitude. Involved rates are calculated with the statistical model where the choice of an α-optical-model potential (αOMP) leads to such a poor precision. The first experiment on ^{87}Rb(α, xn) reactions at weak r-process energies is reported here. Total inclusive cross sections were assessed at $E_{\mathrm{c.m.}} = 8.1-13$ MeV (3.7−7.6 GK) with the active target MUlti-Sampling Ionization Chamber. With an $N = 50$ seed nucleus, the measured values agree with statistical model estimates using the αOMP `Atomki-V2`. A reevaluated reaction rate was incorporated into new nucleosynthesis calculations, focusing on ν-driven ejecta conditions known to be sensitive to this specific rate. These conditions were found to fail to reproduce the lighter heavy element abundances in metal-poor stars.

Unified Astronomy Thesaurus concepts: Core-collapse supernovae (304); Isotopic abundances (867); Nuclear astrophysics (1129); Nucleosynthesis (1131); R-process (1324); Nuclear physics (2077); Nuclear reaction cross sections (2087)

1. Introduction

The oldest metal-poor stars in the Milky Way and in close dwarf galaxies have been investigated over the past decade to bring forth the presence of elements heavier than iron. At these sites, the observed chemical abundances (A. Frebel 2018; B. Côté et al. 2019; M. Reichert et al. 2020) hint that the rapid neutron capture process (D. M. Siegel 2022), expected to produce half of nuclei beyond Fe, should take place in early galactic ages. An active site of this nucleosynthesis has been recently found with the observation of r-process elements in the kilonova following a binary neutron star merger (NSM; D. Kasen et al. 2017; S. Smartt et al. 2017; D. Watson et al. 2019). However, it occurs in galactic evolution too rarely and too late to explain the observed chemical abundances in old stars (B. Côté et al. 2019; C. Kobayashi et al. 2023). Other explosive stellar environments like magnetorotationally driven supernovae (C. Winteler et al. 2012; N. Nishimura et al. 2017; M. Reichert et al. 2021, 2022), collapsars (D. M. Siegel et al. 2019), and neutrino (ν)-driven winds in core-collapse supernovae (CCSNe; C. J. Hansen et al. 2014; C. J. Horowitz et al. 2019) are being investigated.

An enhancement of the elements around the first r-process peak, with $Z = 38-47$, was also observed in a subset of metal-poor stars (C. Sneden et al. 2008; L. Mashonkina et al. 2010; P. Schwerdtfeger et al. 2020). These abundance patterns, e.g., Figure 7 (P. Schwerdtfeger et al. 2020) and Table 2 (A. Psaltis et al. 2022, 2024), call for an additional mechanism that must occur in early galactic ages. Two have been put forward: the weak r-process (F. Montes et al. 2007; Y.-Z. Qian & G. J. Wasserburg 2007; N. Izutani et al. 2009; A. Arcones & F. Montes 2011; J. Bliss et al. 2017, 2018, 2020; A. Psaltis et al. 2022), also known as the α-process (B. S. Meyer et al. 1992), and the neutrino-proton process (νp-process; C. Fröhlich et al. 2006; N. Nishimura et al. 2019). Both are expected to take place in ν-driven ejecta of stellar explosions like CCSNe or

NSMs, depending on the neutron richness of the ejected material. We focus here on the weak *r*-process in ν-driven winds of CCSNe.

In the aftermath of the collapse, temperature decreases while the neutron-rich matter is expanding away from the compact neutron star, and at some point, the nuclear statistical equilibrium breaks down. Regardless of the thermodynamic conditions (expansion timescale, entropy, electron fraction) in these extreme winds, parametric one-dimensional modeling studies (J. Bliss et al. 2017, 2018, 2020) show that (i) radiative *n*-capture reactions are balanced by their reciprocal photodisintegration reactions, (ii) β decays occur more slowly than the expansion timescale of tens of milliseconds, and (iii) $(\alpha, 1n)$ and $(\alpha, 2n)$ reactions are faster to fall out of equilibrium than other α-induced and *p*-induced reactions at temperatures of 2−5 GK. Hence, the nucleosynthesis pathway should stay relatively close to stability, and the nuclear reaction flow toward the elements from Fe to Mo should be driven by (α, xn) reactions where $x = 1$, 2 are the typical cases. Several sensitivity studies (J. Bliss et al. 2018, 2020; A. Psaltis et al. 2022, 2024) have shown that model-to-observation comparisons of abundances around Sr in metal-poor stars are currently inadequate to firmly constrain the thermodynamic conditions of the ν-driven ejecta. This is mainly due to the variations resulting from the uncertainties of (α, xn) reaction rates, which have been poorly measured so far.

Without experimental information, (α, xn) reaction rates are estimated within the Hauser–Feshbach framework (W. Hauser & H. Feshbach 1952; T. Rauscher & F.-K. Thielemann 2000). This model is justified for the mass region of interest and the involved stellar temperatures ($T > 1$ GK), which correspond to the energy region of high nuclear level density in the compound nucleus. Since the decay of the latter is independent of its formation mechanism, the probability that the (α, xn) reaction occurs can be expressed as $\sigma(\alpha, xn) \approx T_{\alpha,0}\frac{T_{xn}}{\sum T_i}$, i.e., the product of the transmission coefficient of the α particle into the seed nucleus ($T_{\alpha,0}$) and the transmission coefficient of the *xn*-exit channel (T_{xn}) that is normalized to all exit channels ($\sum T_i$). The open exit channels are γ-rays and multiple particles (p, n, $2n$, α...). However, at weak *r*-process energies located far above the *n* emission threshold, *xn*-exit channels dominate, and so, the $\frac{T_{xn}}{\sum T_i}$ term reduces to 1. Hence, only the $T_{\alpha,0}$ coefficient is relevant for statistical model estimates of (α, xn) cross sections.

The $T_{\alpha,0}$ coefficient is derived from an α-optical-model potential (αOMP); see, e.g., P. Mohr et al. (2021). Several αOMPs are available, to quote the standard ones (L. McFadden & G. Satchler 1966; M. Nolte et al. 1987; P. Demetriou et al. 2002; A. Koning & J. Delaroche 2003 with the folding approach; S. Watanabe 1958; V. Avrigeanu et al. 2014; P. Mohr et al. 2021). Deviations between reaction rates of 1 to 2 orders of magnitude have been observed while testing different αOMPs. This is illustrated in Figure 1, where several ^{87}Rb$(\alpha, 1n)^{90}$Y reaction rates, normalized to the referenced values of `ReaclibV2.2` (R. H. Cyburt et al. 2010), are presented along temperatures relevant for the weak *r*-process. The reaction rates were calculated with the code `Talys` (A. Koning et al. 2023), where only the chosen αOMP was varied. Note that the ratio resulting from the αOMP (L. McFadden & G. Satchler 1966; solid cyan curve in Figure 1) deviates from unity, even though the same αOMP was used for the reaction rate calculations in `ReaclibV2.2` (R. H. Cyburt et al. 2010), but with the statistical model code `NON-SMOKER` (T. Rauscher & F.-K. Thielemann 2001), and technical differences exist between the two codes.

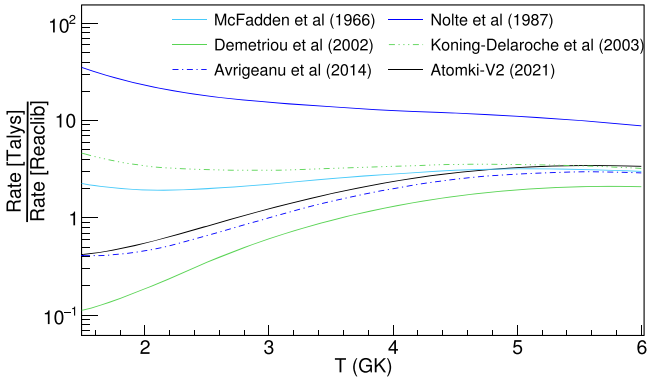

Figure 1. Ratio between the ^{87}Rb$(\alpha, 1n)^{90}$Y reaction rate calculated with the `Talys` code (A. Koning et al. 2023) and the rate from `ReaclibV2.2` (R. H. Cyburt et al. 2010) along temperatures where (α, xn) reactions impact the nucleosynthesis occurring in CCSNe ν-driven winds. Standard αOMPs were considered to calculate the reaction rate, i.e., those from L. McFadden & G. Satchler (1966) shown in solid cyan, from M. Nolte et al. (1987) shown in solid blue, from P. Demetriou et al. (2002) with the dispersive mode shown in solid green, from nucleon potential (A. Koning & J. Delaroche 2003) with the folding approach (S. Watanabe 1958) shown in dotted green, from V. Avrigeanu et al. (2014) shown in dotted blue, and from P. Mohr et al. (2021) shown in solid black. The maximal deviations range from a factor 10 at $T = 5$ GK to a factor 100 at $T = 2$ GK.

Measured data allow us to test the statistical model predictions based on available αOMPs for (α, xn) cross sections with the goal to improve the precision of nucleosynthesis calculations for the weak *r*-process. In this respect, statistical model estimates based on the latest αOMP `Atomki-V2` (P. Mohr et al. 2021) appeared to be consistent with some recent measurements performed on stable nuclei located in the weak *r*-process mass region. These are W. Rapp et al. (2008), A. Oprea et al. (2017), T. N. Szegedi et al. (2021), G. G. Kiss et al. (2021), and W.-J. Ong et al. (2022), for which the deviations between experimental and calculated values of $(\alpha, 1n)$ cross sections are within a factor 0.5−2. However, a recent study on ^{88}Sr at $N = 50$ (C. Fougères et al. 2024) measured a cross section that is systematically lower (∼32%) than statistical model estimates with the αOMP `Atomki-V2`. This, together with the general lack of data available on the neutron-rich side to test statistical model predictions, pushes for more nuclear physics measurements.

The comprehensive sensitivity studies of J. Bliss et al. (2020) and A. Psaltis et al. (2022) have identified the key (α, xn) reactions that strongly contribute to the uncertainties of the yields derived from the modeling of CCSNe ν-driven winds. These works have determined which elemental abundances (and by how much) are affected by a given (α, xn) reaction rate under certain thermodynamics conditions in the ν-driven ejecta and thus suggest a selection of experiments that would best help constrain model-to-observation comparisons for abundances in old stars. Such experimental efforts on measuring (α, xn) weak *r*-process cross sections have already started with stable beams (G. G. Kiss et al. 2021; T. N. Szegedi et al. 2021; W.-J. Ong et al. 2022; C. Fougères et al. 2024). Many more, but with unstable neutron-rich beams or targets, have yet to be assessed. Heavy-ion accelerators like ATLAS (US) or FRIB (US) are now enabling such experimental programs at weak *r*-process

energies ($\sim$1−3 MeV/u) thanks to the high intensities available for beams of the desired neutron-rich isotopes.

Among the stable cases of astrophysical relevance that remain to be measured at astrophysical energies, the reaction ^{87}Rb(α, 1n)^{90}Y was found to impact Z = 41, 42, 44, 45 abundances by factors of 2−3 and (Sr/Zr, Y/Zr, Nb/Zr) elemental ratios in a handful of CCSNe ν-driven wind conditions (J. Bliss et al. 2020; A. Psaltis et al. 2022). Located at the closed shell $N = 50$, this should further test statistical model predictions with the up-to-date αOMP `Atomki-V2` (P. Mohr et al. 2021). To our knowledge, ^{87}Rb(α, 1n)^{90}Y cross sections were only measured above the weak r-process energy region ($E_{\rm c.m.} \geqslant 10.52$ MeV, $T \geqslant 5.5$ GK) with uncertainties of $\sim$20% (C. Riley & B. Linder 1964). The reaction ^{87}Rb(α, 2n)^{89}Y open at $T > 5.6$ GK has not been investigated at all. An inclusive measurement of the two reactions would directly constrain the αOMP since the summed contribution of the (α, 1n) and (α, 2n) channels depends solely on the αOMP.

Responding to the need of data at weak r-process energies and of constraints on the αOMP, this work presents the first measurement of the total cross sections of both ^{87}Rb(α, xn) reactions at $E_{\rm c.m.}$ = 8.1−13 MeV ($T \sim$ 3.7−7.6 GK). The inclusive excitation function was measured with the active gaseous technique. The measured cross sections were then compared to statistical model estimates and the ^{87}Rb(α, 1n)^{90}Y reaction rate determined in the temperature range relevant for the weak r-process in CCSNe ν-driven winds. The impact of this newly constrained reaction rate was assessed on $Z \sim 40$ elemental abundances by nucleosynthesis calculations in CCSNe ν-driven ejecta presenting thermodynamic conditions known to be sensitive to this specific rate. The resulting predictions were finally compared to the abundances observed in a set of old stars.

2. Nuclear Experiment

Earlier experimental investigations on (α, 1n) reactions have tested the standard αOMPs in the mass region relevant for the weak r-process (T. N. Szegedi et al. 2021; W.-J. Ong et al. 2022), including at $N = 50$ closed-shell nuclei (C. Angus et al. 2023; C. Fougères et al. 2024), and reported constraints on modeled elemental abundances in CCSNe ν-driven winds (G. G. Kiss et al. 2021). The stellar reaction rates are determined for charged-particle-induced reactions at energies $\simeq$1 MeV above the neutron emission threshold, and so, most attempts aim at directly assessing high cross sections (0.1−100 mb). To quote recent works, this can be achieved through (i) integrated measurements with the active-target technique in inverse kinematics (W.-J. Ong et al. 2022; C. Fougères et al. 2024), or (ii) β-delayed γ-ray measurements with the activation technique in normal kinematics (A. Oprea et al. 2017; G. G. Kiss et al. 2021; T. N. Szegedi et al. 2021), or (iii) recoil-γ-ray prompt coincidence measurements at a mass separator using direct reactions in inverse kinematics (C. Angus et al. 2023). The present work on ^{87}Rb(α, xn) reactions was carried out using the experimental technique (i).

2.1. Method

The active-target technique relies on the detection medium being also the target material. Cross sections are straightforwardly measured while detecting the nuclei of both the entrance and exit channels of the reaction. This technique presents many advantages: an increased target thickness, a detection efficiency of $\sim$100%, and a self-normalization of the cross section. In the case of α-induced reactions, the technique can be employed in inverse kinematics with active helium-gaseous targets being ionization chambers (M. L. Avila et al. 2017; J. Johnstone et al. 2021; D. Blankstein et al. 2023), time-projection chambers (B. Mauss et al. 2019; Y. Ayyad et al. 2020; E. Koshchiy et al. 2020), or arrays that combine gaseous and semiconductor detectors (E. Koshchiy et al. 2017). The excitation function is probed at different center-of-mass energies ($E_{\rm c.m.}$), while the incident monoenergetic beam is slowing down in the gaseous volume. The reachable range and resolution in $E_{\rm c.m.}$ are governed by incident beam energy, gas pressure, and detector segmentation. Most high-profile seed nuclei in explosive stellar nucleosynthesis are radioactive short-lived elements. The inverse kinematics method used here allows us to investigate them thanks to the delivered radioactive beams.

Depending on the detector sensitivity, the experiment focuses on selecting the heavy recoils or light ejectiles as well as following energy losses or reconstructing reaction vertices and kinematics in order to identify the reaction channel of interest. Since energy loss of ions in matter varies as the square of the atomic number, (α, xn) reactions on $Z \sim 40$ nuclei can be observed via the first method: the measurement of heavy-ion energy losses as they pass through the active gaseous volume. Due to the $Z + 2$ change between the beam and the heavy recoil, a sharp local increase in energy loss is a signature of a reaction occurring. With electrically segmented (stripped) detectors in a single direction (P. Carnelli et al. 2015; J. Johnstone et al. 2021; D. Blankstein et al. 2023), the search for (α, xn) events may follow

1. the *PID method*—a global analysis that looks at energy losses summed over several strips $\Delta E - E_{\rm total}$, similar to the Particle IDentification (PID) with silicon detectors and their variants;
2. the *Traces method*—a local analysis that tracks energy loss per strip.

It is sufficient to analyze energy losses relative to the averaged value found for the beam in order to identify reaction events. However, the absolute energy losses of the beam particles must be known to determine the center-of-mass energies associated with the reaction of interest. The precision in the determination of the beam energy losses directly impacts the energy resolution of the measured excitation function. Energy losses of heavy ions in matter can be estimated with Monte Carlo calculations that integrate tabulated stopping powers. However, large deviations (>10%) have been observed at low energies between tables from standard libraries (F. Hubert et al. 1990; J. F. Ziegler et al. 2010; H. Weick et al. 2018). Hence, performing also a measurement of the beam energy losses in the gaseous detector is essential in active-target experiments that aim at assessing cross sections.

The technique described here was chosen to determine the ^{87}Rb(α, xn) reaction cross sections. Guided by past successful experiments (M. L. Avila et al. 2016, 2017; W.-J. Ong et al. 2022; C. Fougères et al. 2024), the measurement was carried out in inverse kinematics at ATLAS accelerator with the electrically segmented MUlti-Sampling Ionization Chamber (MUSIC; P. Carnelli et al. 2015).

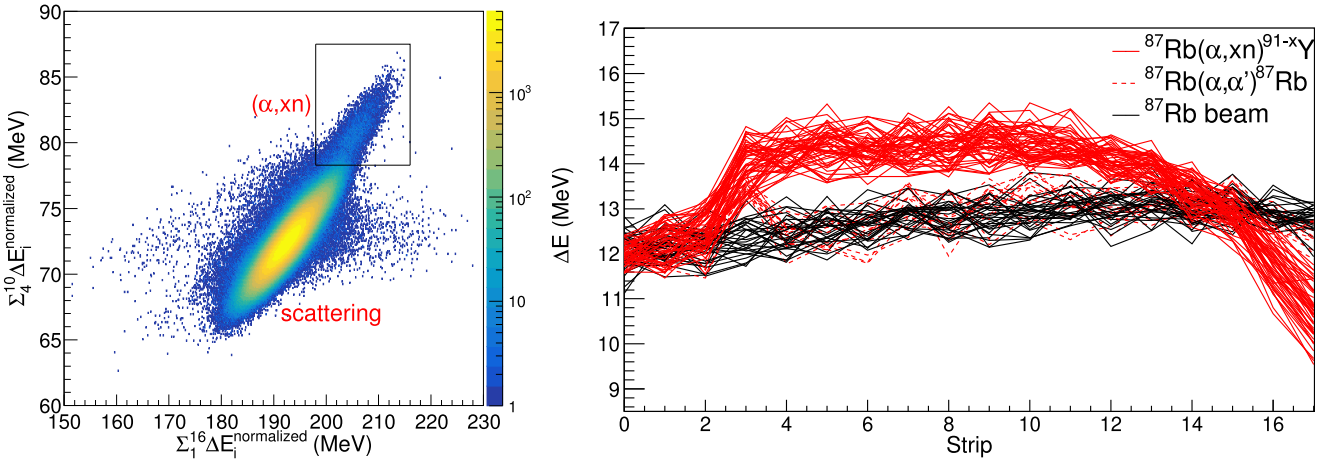

Figure 2. Application of the *PID method* (left) and *Traces method* (right) to identify and quantify (α, xn) reactions occurring in strip 3 of the MUSIC detector. Left panel: sums of energy losses ($\sum_1^{16}\Delta E_i^{\text{normalized}}$, $\sum_4^{10}\Delta E_i^{\text{normalized}}$) are shown for events selected on an ^{87}Rb incoming beam and a sharp increase in energy loss measured in strip 3. The energy losses per strip were normalized to the averaged value of 12 MeV found for the ^{87}Rb beam. The isolated region at $\sum_4^{10}\Delta E_i^{\text{normalized}} \sim 82$ corresponds to (α, xn) events, and scattering events are noticed below. Right panel: individual traces of calibrated energy losses ΔE along the strip number are shown for the unreacted beam (black curves), the (α, xn) (solid red curves), and few (α, α') at low angles (dotted red curves) reactions. The (α, xn) events were obtained with a cut applied on the associated region in the *PID* plot (left) and with energy losses in strip 17 having to be less than 12.5 MeV (below beam energy losses).

2.2. Setup

The ^{87}Rb stable beam delivered by the Argonne Tandem Linac Accelerator System ATLAS had a charge state of 17^+, an energy of 4.61(1) MeV/u, and an average intensity of 3.7×10^4 pps. The beam energy was measured from the time-of-flight value for three resonator pairs located upstream of the MUSIC detector. The beam purity was assessed from the energy losses observed in the most upstream segment of the detector. A single contaminant was observed with an intensity of about 1/7 that of the requested beam. It was $^{51}V^{10+}$ considering the magnetic rigidity matching $^{87}Rb^{17+}$ and the measured energy losses. The MUSIC detector was filled with pure ^{4}He gas at 555 Torr held by Ti foils of 1.30(5) mg cm^{-2} thickness at the entrance and exit sides for the beam. The beam energy loss after passing through the entrance foil was measured to be 46.9(9) MeV. The anode of MUSIC is segmented into 18 strips, indexed from 0 to 17, of equal width (1.578 cm) along the beam axis; see Figure 1 of P. Carnelli et al. (2015). In the data-acquisition system of digital nature (DAQ), each channel was self-triggering, and the beam rate was monitored to ensure the DAQ stability. Less than 10% of pile-up events were observed as expected for such a gaseous detector operated at rates of tens of kHz. In the data analysis, a cut was applied on the energy losses in strips 0 and 1 to fully separate the ^{87}Rb beam events from ^{51}V contaminant events. The amount of ^{87}Rb beam events measured in those two strips was used to normalize (α, xn) cross sections.

Energy losses of ^{87}Rb in the Ti foils and ^{4}He gas were measured with a depleted silicon surface-barrier detector that was mounted downstream of MUSIC. Note that to correct for the pulse-height defects related to heavy ions in Si detectors (B. Wilkins et al. 1971), the energy calibration of the Si detector was performed in-beam by measuring the ^{87}Rb beam at several energies (1.0−4.6 MeV/u) in the Si detector. Regarding the energy loss measurement, the beam energy was measured after the MUSIC detector: first, only with the Ti foils but no gas, and second, the detector was gradually filled with gas where the beam energy at a given pressure was recorded. The measured energy losses were reproduced, i.e., within 2.0%, by Monte Carlo simulations using the mean value of the stopping powers of the ATIMA table in LISE++ (O. Tarasov & D. Bazin 2008) and of the tables in SRIM (J. F. Ziegler et al. 2010).

Overall, the beam energy losses per strip were of 11−13 MeV with a resolution of 8% (FWHM) due to the strip spatial extension. In the active region, several reaction channels were energetically allowed: the Rutherford and inelastic scatterings referred to as (α, α'), the (α, $1n$) channel with $Q_{\text{value}} = -3.75$ MeV, the (α, p) with $Q_{\text{value}} = -3.51$ MeV, and the (α, γ) channel with $Q_{\text{value}} = +4.18$ MeV. Additionally, the (α, $2n$) channel with $Q_{\text{value}} = -10.61$ MeV was opened at the highest energies ($E_{\text{c.m.}} \geqslant 10.87$ MeV). The dominant mechanism is (α, α') with calculated cross sections in excess of 1 barn (estimates from LISE++). Monte Carlo simulations of the setup indicated that (α, p) and (α, γ) events would overlap with (α, xn) events. However, statistical model cross sections from the Talys code revealed that, at present energies, (α, xn) reactions should be favored, by several orders of magnitude (5×10^3−10^5), over (α, p) and (α, γ) reactions. Possible contamination from the latter was thereby negligible compared to the statistical uncertainty (1%−25%) of the measured cross sections. Simulated energy losses of ^{89,90}Y recoils differ by less than 100 keV: this is far below the detector energy resolution. Hence, the $2n$ exit channel could not be isolated from the $1n$ exit channel. The measured inclusive ^{87}Rb(α, xn) cross sections were compared with statistical model cross sections. This allowed us to extract their respective contributions at $E_{\text{c.m.}} \geqslant 10.87$ MeV.

The *PID method* was first employed to identify (α, xn) and scattering events, which occurred in each strip of the MUSIC detector. This is illustrated for the reactions taking place in strip 3 on the left of Figure 2. As detailed previously, two conditions were required: energy losses measured in the first two strips corresponded to ^{87}Rb, and energy losses measured in strip 3 were higher than the ones in strip 2. Two isolated regions are noticed, but the one at higher energies is unambiguously associated to (α, xn) events considering Z of the respective recoils. Then, the *Traces method* was used to count (α, xn) events. Such traces of (α, xn) reactions occurring in strip 3 are shown with the solid red curves on the right of Figure 2. Two

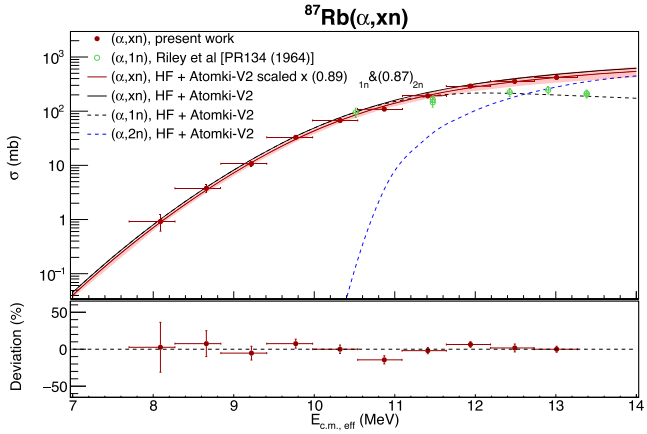

Figure 3. Comparison of ^{87}Rb(α, xn) cross sections as obtained from the present measurement and from the statistical model estimates. The common abscissa is the effective center-of-mass energy ($E_{\mathrm{c.m.,eff}}$). Upper panel: experimental data are shown as red points. The (α, xn) calculated cross sections including the αOMP `Atomki-V2` (P. Mohr et al. 2021; black curve) are dominated by the (α, $1n$) channel (dotted black curve) at low energy $E_{\mathrm{c.m.,eff}} < 11$ MeV. The (α, $2n$) channel (dotted blue curve) starts to contribute (>1%) at $E_{\mathrm{c.m.,eff}} > 10.8$ MeV and dominates at high energy $E_{\mathrm{c.m.,eff}} > 13.5$ MeV. The calculations scaled to experimental data are shown (dotted red curve). This corresponds to the best fit ($\chi^2/ndf = 0.92$) of the weighted sum of the (α, $1n$) and (α, $2n$) calculations to measurements: the deviations are of 0.89(9) and 0.87(14), respectively. Statistical model estimates, only 10% higher than measurements, well reproduce the ^{87}Rb (α, xn) cross sections at $E_{\mathrm{c.m.,eff}} = 8-13$ MeV. The scaled calculations allow to assess cross sections at lower astrophysical energies ($T \leqslant 3.7$ GK). Uncertainty contributions of the measured cross sections are detailed in the text and Table 2 (Appendix). The colored band corresponds to the 3σ uncertainty of the fit for the scaled calculations. Past work on ^{87}Rb(α, $1n$)^{90}Y by C. Riley & B. Linder (1964) is presented (green points). Lower panel: deviations between scaled calculations and measured data scatter around 0% $\pm$ 10% and are not energy dependent.

additional conditions were used here, namely, a cut applied on the (α, xn) region (Figure 2, left) and energy losses in the last strip 17 lower than the values of the beam, i.e., <12.5 MeV. The second was due to the fact that (α, xn) recoils, with a Bragg peak upstream of the beam Bragg peak (strip 13−14), lost less energy in the last strips of MUSIC than beam-like nuclei. The boundaries of the cut were obtained by fitting the projections on the axes of Figure 2 (left) with a distribution of two Gaussian peaks. Several traces of unreacted beam events (black curves) and of beam-like scattering events at low angles (dotted red curves) are also presented on the right of Figure 2. Similarly to W.-J. Ong et al. (2022), scattering reactions at large angles were observed with a higher variation of ΔE than (α, xn) reactions.

2.3. Results

The total cross sections of the ^{87}Rb(α, xn) reactions are presented along the measured effective center-of-mass energies ($E_{\mathrm{c.m.,eff}}$) of 8.09–13.01 MeV in Figure 3 and detailed in Appendix A. To determine $E_{\mathrm{c.m.,eff}}$, the center-of-mass energies deduced from the measurement of the beam energy losses in the MUSIC detector were corrected for the thick-target yield (T. N. Szegedi et al. 2021). Shown with the red points, horizontal (energy) uncertainties of the measured cross sections correspond to the spatial extension of the strip, and vertical uncertainties include both statistical and systematic contributions. The latter comprises the impact of independently varying the conditions applied in the analysis to select the ^{87}Rb beam and identify (α, xn) events as well as the uncertainty in the gas pressure (1 Torr). These conditions were modified by $\pm$10%, i.e., the energy resolution of MUSIC (3σ). Note that at low energies, the systematic contribution strongly increased because the (α, $1n$) and (α, α') channels became more entangled in both the *PID method* and *Traces method*. Due to the too small difference in Z between Rb and Y relative to the total atomic number, the above effect puts a low-energy limit on the present setup to assess (α, xn) weak r-process cross sections.

The measured cross sections are compared to statistical model cross sections in Figure 3 (upper panel). Calculated (α, $1n$) and (α, $2n$) cross sections were obtained with the `Talys` code (A. Koning et al. 2023) using the αOMP `Atomki-V2` (P. Mohr et al. 2021). The results, shown as the dotted black and blue curves, respectively, were summed up to obtain the black curve representing the (α, xn) cross sections (black curve). A fit was then performed between the measurement and the weighted sum of the (α, $1n$) and (α, $2n$) calculations, and the best result (dotted red curve) was obtained for a relative deviation of 0.89(9) and 0.87(14), respectively. The observed deviations were found to be consistent between the two exit channels, i.e., they are equal within uncertainties. This was expected since both cross sections are governed by the same αOMP. It should be noted that using a scaling factor per exit channel or a common factor of 0.88 resulted in negligible changes in the associated reaction rate. This new experimental result supports the use of αOMP `Atomki-V2` to reliably predict (α, xn) cross sections at astrophysical energies in weak r-process. The results of the ^{87}Rb(α, $1n$)^{90}Y reaction measured at high energy by C. Riley & B. Linder (1964) are also shown in Figure 3 (green points). Agreeing with the present work at $E_{\mathrm{c.m.,eff}} = 10.5$ MeV where the ($2n$) exit channel is suppressed, it confirms the robustness of statistical model estimates based on αOMP `Atomki-V2`.

Once scaled, the (α, xn) calculated cross sections were found to differ only by $\pm$10% in comparison to the experimental data; see Figure 3 (lower panel). No systematic trend was noticed along $E_{\mathrm{c.m.,eff}}$. The energy dependence of the experimental data was found to be properly reproduced by statistical model estimates. Therefore, information at energies lower than measured values could be assessed by using the derived constant scaling factor of 0.89(9) to the lowest energies for the ^{87}Rb(α, $1n$)^{90}Y reaction of interest.

Looking at the reduced cross section (σ_{red}) and energy (E_{red}) (P. R. S. Gomes et al. 2005; P. Mohr et al. 2013) allows to directly compare total cross sections of charged-particle reactions whatever the beam, target, and energy are. These two parameters are given by $\sigma_{\mathrm{red}} = \frac{\sigma}{(A_{\mathrm{beam}}^{1/3} + A_{\mathrm{target}}^{1/3})^2}$ and $E_{\mathrm{red}} = \frac{E_{\mathrm{c.m.}}(A_{\mathrm{beam}}^{1/3} + A_{\mathrm{target}}^{1/3})}{Z_{\mathrm{beam}} Z_{\mathrm{target}}}$. A common trend was observed for α-induced reactions around $A \sim 100$ in P. Mohr et al. (2013). This is illustrated in Figure 4, where the result of the $\alpha + {}^{87}$Rb reaction fits well to this trend, similarly to several nuclei with $N = 50$. If confirmed to be the case for even more nuclei, this trend may also be of use to infer weak r-process cross sections not yet measured.

3. Astrophysical Implications

3.1. Thermonuclear Reaction Rates

The ^{87}Rb(α, $1n$)^{90}Y cross sections were measured at the energies corresponding to the Gamow temperatures of 3.7–7.6 GK. Calculations of the associated thermonuclear reaction rate were performed with the code `EXP2RATE` (T. Rauscher 2025). They included the cross sections from

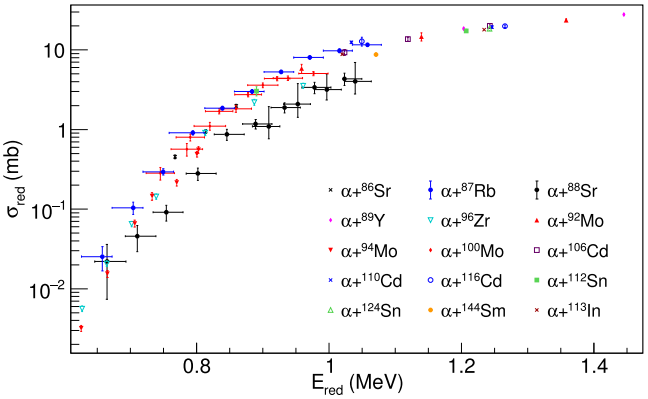

Figure 4. Evolution of the reduced cross section (σ_{red}) as a function of the reduced energy (E_{red}) for $A \approx 86-144$ nuclei produced in α-induced reactions at low energy from P. Mohr et al. (2013), A. Oprea et al. (2017), G. G. Kiss et al. (2021), W. Rapp et al. (2008), W.-J. Ong et al. (2022), and C. Fougères et al. (2024). Present results on ^{87}Rb (blue circles) follow the apparent trend.

Table 1
Low, Recommended, and High Thermonuclear Rates of the ^{87}Rb(α, 1n)^{90}Y Reaction, in Units of cm^3 mol^{-1} s^{-1}, for Temperatures Relevant for the Weak r-process

T (GK)	Low	Recommended	High
1.6	6.58×10^{-14}	1.13×10^{-13}	1.93×10^{-13}
2.0	6.66×10^{-11}	1.09×10^{-10}	1.80×10^{-10}
2.5	3.51×10^{-8}	5.27×10^{-8}	7.91×10^{-8}
3.0	3.95×10^{-6}	5.41×10^{-6}	7.42×10^{-6}
3.5	1.61×10^{-4}	2.05×10^{-4}	2.62×10^{-4}
4.0	3.20×10^{-3}	3.88×10^{-3}	4.70×10^{-3}
4.5	3.75×10^{-2}	4.40×10^{-2}	5.15×10^{-2}
5.0	2.93×10^{-1}	3.37×10^{-1}	3.87×10^{-1}
5.5	1.95	2.17	2.39
6.0	7.45	8.39	9.44

statistical model estimates based on the Atomki-V2 αOMP (P. Mohr et al. 2021) scaled by the constant factor of 0.89(9) deduced from the experiment. Recommended values of the ^{87}Rb(α, 1n)^{90}Y reaction rate at temperatures where the weak r-process impacts the nucleosynthesis in ν-driven ejecta of CCSNe are reported in Table 1.

The lower and higher limits of the reaction rate were derived from uncertainties of the scaling factor that range from $\sim$10% at measured energies ($E_{c.m.} \gtrsim 8$ MeV) to a factor 2 at the threshold energy of the reaction ($E_{c.m.} = 3.8$ MeV). The ^{87}Rb(α, 1n)^{90}Y reaction rate was found to be exceeded by the ^{87}Rb(α, 2n)^{89}Y reaction rate at $T > 8$ GK. In similar calculations to assess the rate of the latter reaction, the statistical model cross sections were weighted by the constant scaling factor found for the 2n exit channel (0.87(14)). Note that the tabulated rates of the two reactions for each value of the default temperature grid of the `Talys` code are given in Appendix B.

The evolution of the recommended rate of the ^{87}Rb(α, 1n)^{90}Y reaction as a function of temperature is shown in Figure 5 (violet curve). The status prior to the measurement, shown as the cyan band, was obtained from calculations that included standard αOMPs (see Figure 1) and low (high) limits corresponding to P. Demetriou et al. (2002; M. Nolte et al. 1987). The precision of the ^{87}Rb(α, 1n)^{90}Y reaction rate is drastically increased at $T \sim 2-5$ GK, i.e., current uncertainties based on experimental data are $\sim$65%−15%, whereas prior uncertainties based on

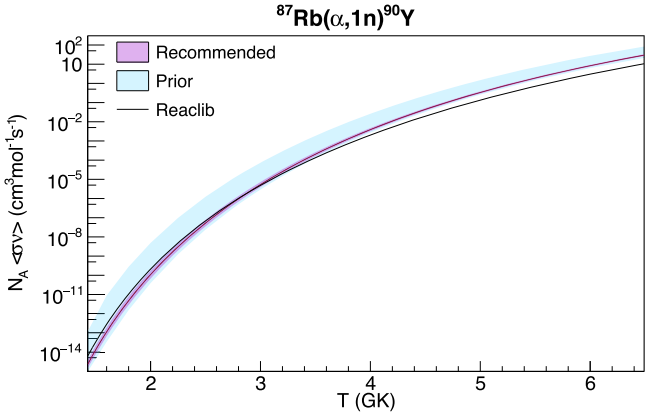

Figure 5. Evolution of the thermonuclear reaction rate of ^{87}Rb(α, 1n)^{90}Y as a function of temperature relevant for the weak r-process. The recommended reaction rate (violet curve) was determined using the code `EXP2RATE` based on cross sections from `Talys+Atomki-V2` scaled by the constant factor of 0.89. Resulting uncertainties are $\sim$65%−15% at $T \sim 2-5$ GK. The prior rate, shown as the cyan band, was evaluated from `Talys` calculations based on standard αOMPs (Figure 1, uncertainties of 100–10). The reaction rate from `ReaclibV2.2` (black curve) agrees with the rate here reevaluated (within a factor of 2).

statistical model calculations are a factor of 100–10. The referenced rate from `ReaclibV2.2` (R. H. Cyburt et al. 2010) is also given in Figure 5 (black curve). At weak r-process temperatures, the two rates agree within a factor of 2. This is in line with the initial development where the `ReaclibV2.2` rate was observed to be close to statistical model estimates based on the `Atomki-V2`αOMP (see Figure 1).

3.2. Elemental Abundances

The impact of the newly constrained ^{87}Rb(α, 1n)^{90}Y reaction rate on the weak r-process abundances around $Z \sim 40$ was studied via extensive nucleosynthesis calculations. We used the four thermodynamic conditions MC12, MC13, MC15, and MC16 from J. Bliss et al. (2020; see Table 4), which have shown sensitivity to the ^{87}Rb(α, 1n)^{90}Y reaction rate in the works of J. Bliss et al. (2020) and A. Psaltis et al. (2022), with the same reaction network setup as in A. Psaltis et al. (2022). With the exception of MC13, the electron fraction is high, and two trajectories (MC15, MC16) have a high entropy ($s > 100\, k_B$ nucleon^{-1}).

Figure 6 shows the nucleosynthesis results for each of the aforementioned weak r-process thermodynamic conditions. Each panel displays the final isotopic pattern after 1 Gy using the `ReaclibV2.2` rate for the ^{87}Rb(α, 1n)^{90}Y reaction as a baseline case (black line). Additionally, we calculated the range of abundances using the prior ^{87}Rb(α, 1n)^{90}Y reaction rate based on standard αOMPs (cyan shaded region). Furthermore, we repeated the calculations using the new experimental reaction rate (Table 3) together with its constrained uncertainty (magenta shaded region). The use of the experimental reaction rate for ^{87}Rb(α, 1n)^{90}Y reduces the uncertainty in the yields of the $A > 90$ species to a few percent. By comparison, the use of the prior rate results in uncertainties of $\sim$50% for some conditions.

We also compared the new nucleosynthesis results with the elemental abundance ratios—Sr/Zr and Y/Zr—of metal-poor stars that exhibit an excess of Sr–Ag relative to solar values, as reported by A. Psaltis et al. (2022). Despite showing some sensitivity to the uncertainty in the ^{87}Rb(α, 1n)^{90}Y reaction rate, the four astrophysical conditions we investigated were

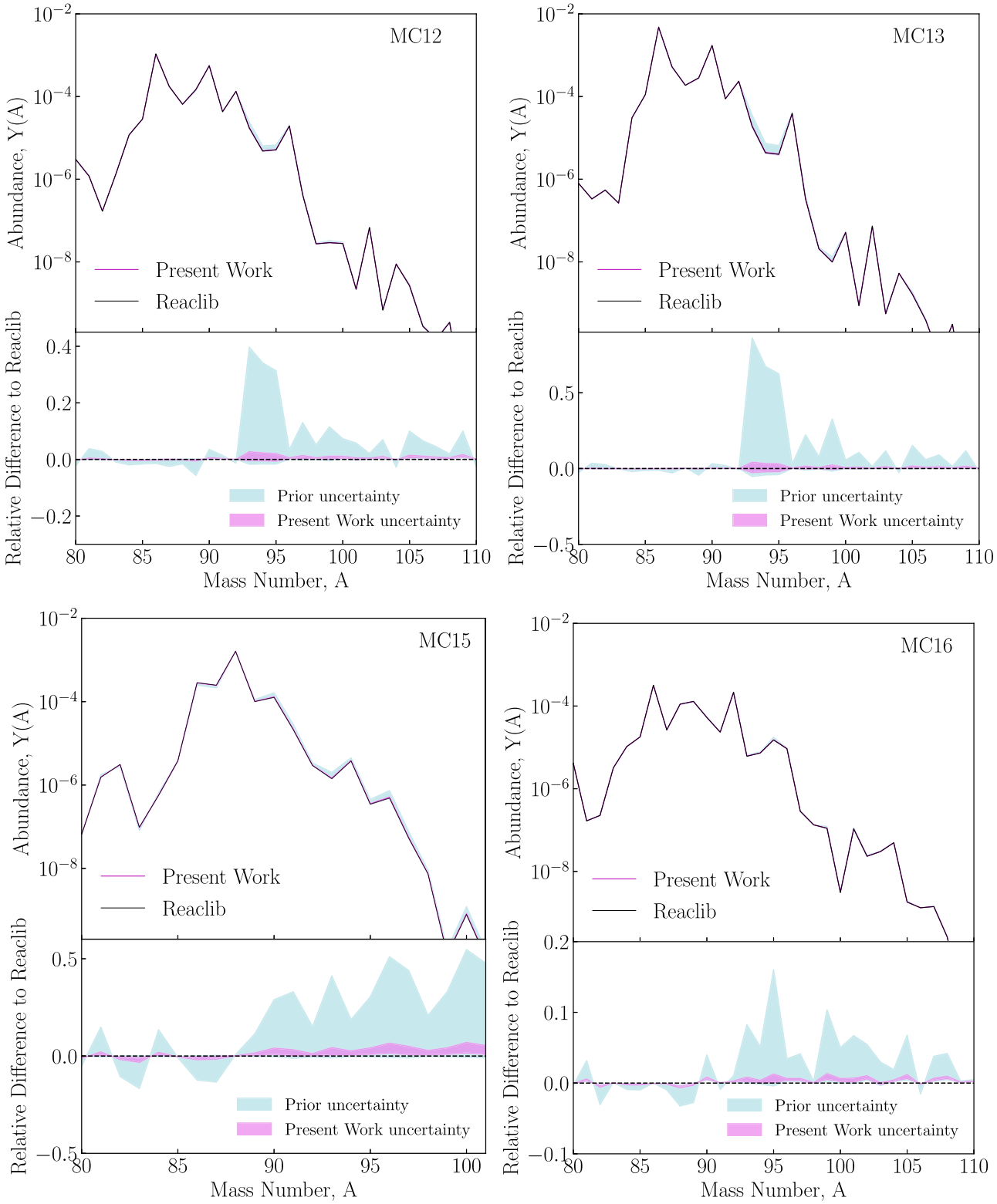

Figure 6. Isotopic abundance patterns for four different sets of ν-driven ejecta corresponding to the conditions MC12, MC13, MC15, and MC16 detailed in Table 4 (Appendix). The calculations use the setup of A. Psaltis et al. (2022). Each panel shows the abundance pattern as a function of mass number A for three cases: calculations using the `ReaclibV2.2` ^{87}Rb(α, 1n)^{90}Y rate (black), the rate of the present work (magenta), and the previously recommended rate (cyan). The bottom panels illustrate the relative differences between each calculation and the one using the `ReaclibV2.2` rate. The new constrained reaction rate reduces the uncertainty in isotopic production for $A > 90$. See the text for further details.

unable to reproduce the observed abundance ratios, consistent with the findings of A. Psaltis et al. (2022). However, as illustrated in Figure 7, our current experiment has significantly reduced the uncertainty in these abundance ratios. This improvement in one of the major nuclear physics uncertainties allows us to confidently rule out these conditions of the ν-driven winds as potential candidates for reproducing the observed abundance ratios in these metal-poor stars.

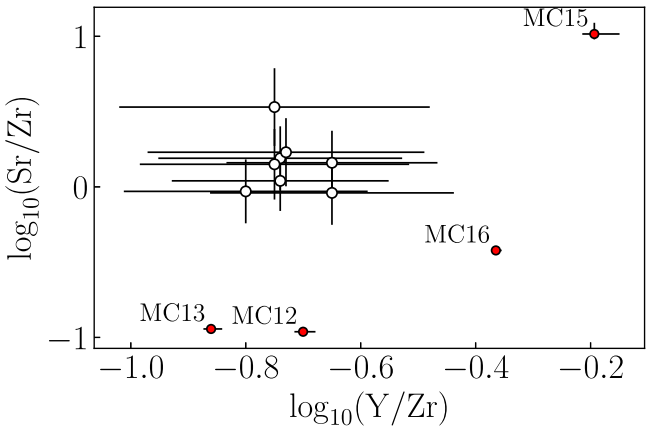

Figure 7. Comparison between nucleosynthesis models and elemental abundance ratios of metal-poor stars from the compilation of A. Psaltis et al. (2022). The four astrophysical conditions are presented in Table 4 (Appendix). The error bars correspond to the uncertainty for the ratios based on the prior ^{87}Rb(α, 1n)^{90}Y reaction rate. The calculations with the new experimentally constrained rate are presented as the red points. The new uncertainty based on the present ^{87}Rb(α, 1n)^{90}Y reaction rate is smaller than the size of the points. The selected ejecta conditions fail to reproduce abundance observations in several metal-poor stars.

4. Conclusion

The ^{87}Rb(α, 1n)^{90}Y reaction has been reported to impact $Z \sim 40$ abundances, which should be produced by the weak r-process ongoing in ν-driven winds after CCSNe. The present work provides the first experimental insight into this reaction at astrophysical temperatures. The total cross sections of ^{87}Rb(α, xn) reactions were measured at $T = 3.7-7.6$ GK with the active gaseous target MUSIC. Measured values were found to be highly consistent with statistical model estimates based on the αOMP `Atomki-V2`. This led to a robust reevaluation of the thermonuclear rates of the ^{87}Rb(α, 1n)^{90}Y and ^{87}Rb(α, 2n)^{89}Y reactions. The experimental inputs indeed constrained, by 2 to 3 orders of magnitude, the ^{87}Rb(α, 1n)^{90}Y reaction rate at weak r-process temperatures, i.e., the present uncertainties of 15%−65% are to be compared with the prior uncertainties of 10−100. This test of the input of the statistical model calculations for cases at $N = 50$ further supports the potential `Atomki-V2` in its predictive power of α-induced reaction cross sections. In the near future, more and more constraints on (α, xn) weak r-process reactions are expected from the ongoing experimental program with the MUSIC detector harvesting the neutron-rich beams available at the ATLAS and FRIB accelerators.

The impact of the reevaluated rate of the ^{87}Rb(α, 1n)^{90}Y reaction was assessed in detailed nucleosynthesis calculations for different ν-driven trajectories of various thermodynamics conditions, introduced in previous impact studies (J. Bliss et al. 2020; A. Psaltis et al. 2022). Under the investigated conditions, the experimental reaction rate reduces the production uncertainty of $A > 90$ species to $\approx$10%. As expected, from previous studies, our comparison with observed abundance ratios did not yield any matches. However, it has helped eliminate these ν-driven conditions as the candidates, narrowing down the possibilities for reproducing the peculiar abundance patterns in the Sr–Ag region observed in metal-poor stars in the Galaxy.

Acknowledgments

The authors thank the support of the ATLAS beam and detection physicists. This material is based upon work supported by the U.S. Department of Energy, Office of Science, Office of Nuclear Physics, under Contract No. DE-AC02-06CH11357. This research used resources of Argonne National Laboratory's ATLAS facility, which is a DOE Office of Science User Facility. A.P. acknowledges support from the U.S. Department of Energy, Office of Science, Office of Nuclear Physics, under Award Number DE-SC0017799 and Contract Nos. DE-FG02-97ER41033 and DE-FG02-97ER41042. P.M. would like to acknowledge the support of NKFIH (grant K134197). S.B. acknowledges support from the Institute for Basic Science, South Korea (IBS), under grant No. IBS-R031-D1.

Appendix A
Cross-section Data

The measured cross sections of the ^{87}Rb(α, xn) reactions are detailed in Table 2 where values and associated uncertainties are listed along the measured effective center-of-mass energies. The corresponding Gamow temperatures are also mentioned.

Table 2
Reported Are the Cross Sections ($\sigma_{(\alpha,xn)}$) of the ^{87}Rb(α, xn) Reactions Measured for a Given Effective Center-of-mass Energy ($E_{\mathrm{c.m.,eff}}$)

$E_{\mathrm{c.m.,eff}}$[a] (MeV)	Range[b]	Gamow Temperature (GK)	$\sigma_{(\alpha,xn)}$ (mb)	Uncertainties (%)	
				Statistical	Systematic
$13.01^{+0.26}_{-0.28}$	[13.27, 12.73]	7.6	420(17)	1.01	3.95
$12.49^{+0.24}_{-0.30}$	[12.73, 12.19]	7.2	355(19)	1.13	5.37
$11.94^{+0.25}_{-0.30}$	[12.19, 11.64]	6.7	291(11)	1.28	3.71
$11.41^{+0.23}_{-0.32}$	[11.64, 11.09]	6.2	192(8)	1.62	4.32
$10.87^{+0.22}_{-0.33}$	[11.09, 10.54]	5.8	109(6)	2.19	5.40
$10.32^{+0.22}_{-0.33}$	[10.54, 9.98]	5.4	67.4(38)	2.81	4.87
$9.77^{+0.21}_{-0.44}$	[9.98, 9.41]	5.0	32.9(20)	4.08	4.62
$9.22^{+0.19}_{-0.38}$	[9.41, 8.84]	4.5	10.7(10)	7.24	6.18
$8.66^{+0.18}_{-0.39}$	[8.84, 8.27]	4.1	3.77(66)	12.3	12.4
$8.09^{+0.18}_{-0.39}$	[8.27, 7.70]	3.7	0.92(31)	25.0	23.6

Notes. The uncertainty of $E_{\mathrm{c.m.,eff}}$ includes the contributions of measured energy losses and incident beam energy. The energy range mentioned covers the strip. Statistical and systematic uncertainties of $\sigma_{(\alpha,xn)}$ are given.
[a] At effective strip thickness corrected from the thick-target yield.
[b] From entrance to strip exit.

Appendix B
Tabulated ^{87}Rb(α, xn) Reaction Rate

Recommended, low, and high thermonuclear rates of the ^{87}Rb(α, $1n$)^{90}Y and ^{87}Rb(α, $2n$)^{89}Y reactions are reported for each value of the default temperature grid of the Talys code in Table 3.

Table 3
Recommended, Low, and High Thermonuclear Rates of the ^{87}Rb(α, $1n$)^{90}Y and ^{87}Rb(α, $2n$)^{89}Y Reactions, in Units of cm^3 mol^{-1} s^{-1}, along the Default Temperature Grid of the Talys Code

T (GK)	Recommended	Low (α, $1n$)	High	Recommended	Low (α, $2n$)	High
0.10	$<10^{-30}$	$<10^{-30}$	$<10^{-30}$	$<10^{-30}$	$<10^{-30}$	$<10^{-30}$
0.15	$<10^{-30}$	$<10^{-30}$	$<10^{-30}$	$<10^{-30}$	$<10^{-30}$	$<10^{-30}$
0.20	$<10^{-30}$	$<10^{-30}$	$<10^{-30}$	$<10^{-30}$	$<10^{-30}$	$<10^{-30}$
0.25	$<10^{-30}$	$<10^{-30}$	$<10^{-30}$	$<10^{-30}$	$<10^{-30}$	$<10^{-30}$
0.3	$<10^{-30}$	$<10^{-30}$	$<10^{-30}$	$<10^{-30}$	$<10^{-30}$	$<10^{-30}$
0.35	$<10^{-30}$	$<10^{-30}$	$<10^{-30}$	$<10^{-30}$	$<10^{-30}$	$<10^{-30}$
0.40	$<10^{-30}$	$<10^{-30}$	$<10^{-30}$	$<10^{-30}$	$<10^{-30}$	$<10^{-30}$
0.45	$<10^{-30}$	$<10^{-30}$	$<10^{-30}$	$<10^{-30}$	$<10^{-30}$	$<10^{-30}$
0.50	$<10^{-30}$	$<10^{-30}$	$<10^{-30}$	$<10^{-30}$	$<10^{-30}$	$<10^{-30}$
0.60	$<10^{-30}$	$<10^{-30}$	$<10^{-30}$	$<10^{-30}$	$<10^{-30}$	$<10^{-30}$
0.70	8.62×10^{-30}	5.17×10^{-30}	1.47×10^{-29}	$<10^{-30}$	$<10^{-30}$	$<10^{-30}$
0.80	2.36×10^{-26}	1.41×10^{-26}	4.01×10^{-26}	$<10^{-30}$	$<10^{-30}$	$<10^{-30}$
0.90	1.17×10^{-23}	7.02×10^{-24}	1.99×10^{-23}	$<10^{-30}$	$<10^{-30}$	$<10^{-30}$
1.0	1.77×10^{-21}	1.06×10^{-21}	3.01×10^{-21}	$<10^{-30}$	$<10^{-30}$	$<10^{-30}$
1.2	2.99×10^{-18}	1.73×10^{-18}	5.16×10^{-18}	$<10^{-30}$	$<10^{-30}$	$<10^{-30}$
1.4	1.13×10^{-15}	6.55×10^{-16}	1.95×10^{-15}	$<10^{-30}$	$<10^{-30}$	$<10^{-30}$
1.6	1.13×10^{-13}	6.58×10^{-14}	1.93×10^{-13}	1.21×10^{-26}	7.05×10^{-27}	2.06×10^{-26}
1.8	4.73×10^{-12}	2.80×10^{-12}	7.97×10^{-12}	1.80×10^{-22}	1.07×10^{-22}	3.03×10^{-22}
2.0	1.09×10^{-10}	6.66×10^{-11}	1.80×10^{-10}	2.02×10^{-19}	1.24×10^{-19}	3.33×10^{-19}
2.25	3.63×10^{-9}	2.31×10^{-9}	5.68×10^{-9}	2.31×10^{-16}	1.47×10^{-16}	3.61×10^{-16}
2.5	5.27×10^{-8}	3.51×10^{-8}	7.91×10^{-8}	6.60×10^{-14}	4.40×10^{-14}	9.90×10^{-14}
2.75	6.84×10^{-7}	4.79×10^{-7}	9.76×10^{-7}	6.88×10^{-12}	4.82×10^{-12}	9.81×10^{-12}
3.0	5.41×10^{-6}	3.95×10^{-6}	7.42×10^{-6}	3.37×10^{-10}	2.46×10^{-10}	4.62×10^{-10}
3.25	3.92×10^{-5}	2.98×10^{-5}	5.15×10^{-5}	9.22×10^{-9}	6.78×10^{-9}	1.21×10^{-8}
3.5	2.05×10^{-4}	1.61×10^{-4}	2.62×10^{-4}	1.60×10^{-7}	1.25×10^{-7}	2.04×10^{-7}
3.75	1.00×10^{-3}	8.07×10^{-4}	1.24×10^{-3}	1.92×10^{-6}	1.54×10^{-6}	2.39×10^{-6}
4.0	3.88×10^{-3}	3.20×10^{-3}	4.70×10^{-3}	1.72×10^{-5}	1.41×10^{-5}	2.09×10^{-5}
4.25	1.42×10^{-2}	1.19×10^{-2}	1.69×10^{-2}	1.21×10^{-4}	9.99×10^{-5}	1.45×10^{-4}
4.5	4.40×10^{-2}	3.75×10^{-2}	5.15×10^{-2}	6.90×10^{-4}	5.87×10^{-4}	8.09×10^{-4}
4.75	1.30×10^{-1}	1.12×10^{-1}	1.50×10^{-1}	3.32×10^{-3}	2.85×10^{-3}	3.98×10^{-3}
5.0	3.37×10^{-1}	2.93×10^{-1}	3.87×10^{-1}	1.38×10^{-2}	1.15×10^{-2}	1.62×10^{-2}
5.5	2.17×10^{0}	1.95×10^{0}	2.39×10^{0}	1.66×10^{-1}	1.45×10^{-1}	1.90×10^{-1}
6.0	8.39×10^{0}	7.45×10^{0}	9.44×10^{0}	1.35×10^{0}	1.18×10^{0}	1.53×10^{0}
6.5	3.03×10^{1}	2.70×10^{1}	3.39×10^{1}	7.98×10^{0}	7.10×10^{0}	8.94×10^{0}
7.0	9.28×10^{1}	8.31×10^{1}	1.04×10^{2}	3.63×10^{1}	3.24×10^{1}	4.08×10^{1}
7.5	2.48×10^{2}	2.23×10^{2}	2.77×10^{2}	1.32×10^{2}	1.18×10^{2}	1.47×10^{2}
8.0	3.39×10^{2}	3.05×10^{2}	3.73×10^{2}	3.99×10^{2}	3.58×10^{2}	4.40×10^{2}
8.5	5.65×10^{2}	5.08×10^{2}	6.22×10^{2}	1.02×10^{3}	9.17×10^{2}	1.13×10^{3}
9.0	8.46×10^{2}	7.60×10^{2}	9.31×10^{2}	2.29×10^{3}	2.05×10^{3}	2.52×10^{3}
9.5	1.16×10^{3}	1.04×10^{3}	1.28×10^{3}	4.58×10^{3}	4.10×10^{3}	5.06×10^{3}
10	1.48×10^{3}	1.33×10^{3}	1.63×10^{3}	8.33×10^{3}	7.48×10^{3}	9.17×10^{3}

Appendix C
Astrophysical Conditions Used in Nuclear Network Calculations

Thermodynamic conditions of the CCSNe ν-driven winds used in the nuclear network calculations as obtained from J. Bliss et al. (2020) are detailed in Table 4. The resulting elemental abundance ratios of interest are also mentioned.

Table 4
Astrophysical Conditions of CCSNe ν-driven Winds and Abundances at $Z \sim 40$ Impacted by the ^{87}Rb(α, $1n$)^{90}Y Reaction Rate, as Taken from J. Bliss et al. (2020): The Electron Mass Fraction Y_e, the Entropy per Baryon s, and the Expansion Timescale τ

CCSNe ν-wind Trajectory	Y_e	s (k_B nucleon^{-1})	τ (ms)	$\log_{10}$(Sr/Zr)	$\log_{10}$(Y/Zr)	$\log_{10}$(Nb/Zr)
12	0.48	85	9.7	-0.962 ± 0.001	-0.700 ± 0.001	$-1.630^{+0.056}_{-0.085}$
13	0.43	64	35.9	-0.944 ± 0.001	-0.860 ± 0.001	$-2.030^{+0.099}_{-0.182}$
15	0.48	103	20.4	$1.020^{+0.007}_{-0.006}$	-0.193 ± 0.004	$-2.040^{+0.018}_{-0.023}$
16	0.49	126	15.4	-0.422 ± 0.001	-0.345 ± 0.001	$-1.690^{+0.013}_{-0.016}$

Note. The uncertainty in the elemental ratios is based only on the variation of the ^{87}Rb(α, $1n$)^{90}Y rate within its new experimental uncertainties.

ORCID iDs

C. Fougères https://orcid.org/0000-0002-1236-4739
M. L. Avila https://orcid.org/0009-0002-4051-9627
A. Psaltis https://orcid.org/0000-0003-2197-0797
M. Anastasiou https://orcid.org/0000-0002-3763-714X
H. Jayatissa https://orcid.org/0000-0001-8746-0234
V. Karayonchev https://orcid.org/0000-0002-6497-0175
P. Mohr https://orcid.org/0000-0002-6695-9359
F. Montes https://orcid.org/0000-0001-9849-5555
D. Neto https://orcid.org/0000-0002-5397-7048
F. de Oliveira Santos https://orcid.org/0000-0003-4539-5985
K. E. Rehm https://orcid.org/0009-0009-4827-0863
D. Santiago-Gonzalez https://orcid.org/0000-0003-3125-9907
N. Sensharma https://orcid.org/0000-0002-5046-9451
R. S. Sidhu https://orcid.org/0000-0002-1637-7502
I. A. Tolstukhin https://orcid.org/0000-0002-6631-7479

References

Angus, C., Williams, M., Andreyev, A., et al. 2023, EPJWC, 279, 11003
Arcones, A., & Montes, F. 2011, ApJ, 731, 5
Avila, M. L., Rehm, K. E., Almaraz-Calderon, S., et al. 2016, PhRvC, 94, 065804
Avila, M. L., Rehm, K. E., Almaraz-Calderon, S., et al. 2017, NIMPA, 859, 63
Avrigeanu, V., Avrigeanu, M., & Mănăilescu, C. 2014, PhRvC, 90, 044612
Ayyad, Y., Abgrall, N., Ahn, T., et al. 2020, NIMPA, 954, 161341
Blankstein, D., Bardayan, D., Allen, J., et al. 2023, NIMPA, 1047, 167777
Bliss, J., Arcones, A., Montes, F., & Pereira, J. 2017, JPhG, 44, 054003
Bliss, J., Arcones, A., Montes, F., & Pereira, J. 2020, PhRvC, 101, 055807
Bliss, J., Witt, M., Arcones, A., Montes, F., & Pereira, J. 2018, ApJ, 855, 135
Carnelli, P., Almaraz-Calderon, S., Rehm, K. E., et al. 2015, NIMPA, 799, 197
Cyburt, R. H., Amthor, A. M., Ferguson, R., et al. 2010, ApJS, 189, 240
Côté, B., Eichler, M., Arcones, A., et al. 2019, ApJ, 875, 106
Demetriou, P., Grama, C., & Goriely, S. 2002, NuPhA, 707, 253
Fougères, C., Avila, M. L., Jayatissa, H., et al. 2024, PhRvC, 109, 065805
Frebel, A. 2018, ARNPS, 68, 237
Fröhlich, C., Martínez-Pinedo, G., Liebendörfer, M., et al. 2006, PhRvL, 96, 142502
Gomes, P. R. S., Lubian, J., Padron, I., & Anjos, R. M. 2005, PhRvC, 71, 017601
Hansen, C. J., Montes, F., & Arcones, A. 2014, ApJ, 797, 123
Hauser, W., & Feshbach, H. 1952, PhRv, 87, 366
Horowitz, C. J., Arcones, A., Côté, B., et al. 2019, JPhG, 46, 083001
Hubert, F., Bimbot, R., & Gauvin, H. 1990, ADNDT, 46, 1
Izutani, N., Umeda, H., & Tominaga, N. 2009, ApJ, 692, 1517
Johnstone, J., Kumar, R., Hudan, S., et al. 2021, NIMPA, 1014, 165697
Kasen, D., Metzger, B., Barnes, J., Quataert, E., & Ramirez-Ruiz, E. 2017, Natur, 551, 80
Kiss, G. G., Szegedi, T. N., Mohr, P., et al. 2021, ApJ, 908, 202
Kobayashi, C., Mandel, I., Belczynski, K., et al. 2023, ApJL, 943, L12
Koning, A., & Delaroche, J. 2003, NuPhA, 713, 231
Koning, A., Hilaire, S., & Goriely, S. 2023, EPJA, 59, 131
Koshchiy, E., Blackmon, J., Rogachev, G., et al. 2017, NIMPA, 870, 1
Koshchiy, E., Rogachev, G., Pollacco, E., et al. 2020, NIMPA, 957, 163398
Mashonkina, L., Christlieb, N., Barklem, P. S., et al. 2010, A&A, 516, A46
Mauss, B., Morfouace, P., Roger, T., et al. 2019, NIMPA, 940, 498
McFadden, L., & Satchler, G. 1966, NucPh, 84, 177
Meyer, B. S., Mathews, G. J., Howard, W. M., Woosley, S. E., & Hoffman, R. D. 1992, ApJ, 399, 656
Mohr, P., Fülöp, Z., Gyürky, G., et al. 2021, ADNDT, 142, 101453
Mohr, P., Kiss, G., Fülöp, Z., et al. 2013, ADNDT, 99, 651
Montes, F., Beers, T. C., Cowan, J., et al. 2007, ApJ, 671, 1685
Nishimura, N., Rauscher, T., Hirschi, R., et al. 2019, MNRAS, 489, 1379
Nishimura, N., Sawai, H., Takiwaki, T., Yamada, S., & Thielemann, F.-K. 2017, ApJL, 836, L21
Nolte, M., Machner, H., & Bojowald, J. 1987, PhRvC, 36, 1312
Ong, W.-J., Avila, M. L., Mohr, P., et al. 2022, PhRvC, 105, 055803
Oprea, A., Glodariu, T., Filipescu, D., et al. 2017, EPJWC, 146, 01016
Psaltis, A., Arcones, A., Montes, F., et al. 2022, ApJ, 935, 27
Psaltis, A., Jacobi, M., Montes, F., et al. 2024, ApJ, 966, 11
Qian, Y.-Z., & Wasserburg, G. J. 2007, PhR, 442, 237
Rapp, W., Dillmann, I., Käppeler, F., et al. 2008, PhRvC, 78, 025804
Rauscher, T., & Thielemann, F.-K. 2001, ADNDT, 79, 47
Rauscher, T., 2025 Computer Code EXP2RATE V2.1, http://nucastro.org/codes.html
Rauscher, T., & Thielemann, F.-K. 2000, ADNDT, 75, 1
Reichert, M., Hansen, C. J., Hanke, M., et al. 2020, A&A, 641, A127
Reichert, M., Obergaulinger, M., Aloy, M. A., et al. 2022, MNRAS, 518, 1557
Reichert, M., Obergaulinger, M., Eichler, M., Aloy, M. A., & Arcones, A. 2021, MNRAS, 501, 5733
Riley, C., & Linder, B. 1964, PhRv, 134, B559
Schwerdtfeger, P., Smits, P., & Pyykkö, O. 2020, Nat Rev Chem, 4, 359
Siegel, D. M. 2022, NatRP, 4, 306
Siegel, D. M., Barnes, J., & Metzger, B. D. 2019, Natur, 569, 241
Smartt, S., Chen, T.-W., Jerkstrand, A., et al. 2017, Natur, 551, 75
Sneden, C., Cowan, J. J., & Gallino, R. 2008, ARA&A, 46, 241
Szegedi, T. N., Kiss, G. G., Mohr, P., et al. 2021, PhRvC, 104, 035804
Tarasov, O., & Bazin, D. 2008, NIMPB, 266, 4657
Watanabe, S. 1958, NucPh, 8, 484
Watson, D., Hansen, C., Selsing, J., et al. 2019, Natur, 574, 497
Weick, H., Geissel, H., Iwasa, N., et al. 2018, GSI Sci. Rep., 2018-1, 130
Wilkins, B., Fluss, M., Kaufman, S., Gross, C., & Steinberg, E. 1971, NucIM, 92, 381
Winteler, C., Käppeli, R., Perego, A., et al. 2012, ApJL, 750, L22
Ziegler, J. F., Ziegler, M. D., & Biersack, J. P. 2010, NIMPB, 268, 1818